Obscuration-free pupil-plane phase locking of a coherent array of fiber collimators

Mikhail A. Vorontsov,[1,*] Svetlana L. Lachinova,[2] Leonid A. Beresnev,[3] and Thomas Weyrauch[1]

[1]*School of Engineering, University of Dayton, 300 College Park, Dayton, Ohio 45469, USA*
[2]*Institute for Systems Research, University of Maryland, College Park, Maryland 20742, USA*
[3]*Computational and Information Sciences Directorate, U.S. Army Research Laboratory, Adelphi, Maryland 20783, USA*
**Corresponding author: Mikhail.Vorontsov@udayton.edu*

Received March 30, 2010; revised August 9, 2010; accepted August 11, 2010;
posted August 12, 2010 (Doc. ID 126297); published September 17, 2010

Control methods and system architectures that can be used for locking in phase of multiple laser beams that are generated at the transmitter aperture plane of a coherent fiber-collimator array system (pupil-plane phase locking) are considered. In the proposed and analyzed phase-locking techniques, sensing of the piston phase differences is performed using interference of periphery (tail) sections of the laser beams prior to their clipping by the fiber-collimator transmitter apertures. This obscuration-free sensing technique eliminates the need for a beam splitter being directly located inside the optical train of the transmitted beams—one of the major drawbacks of large-aperture and/or high-power fiber-array systems. Numerical simulation results demonstrate efficiency of the proposed phase-locking methods. © 2010 Optical Society of America

OCIS codes: 010.1080, 010.7350, 140.3290, 140.3298, 140.3510, 220.0220.

1. INTRODUCTION

There has been a growing interest in development of long-range laser beam transmitter systems with sparse (conformal) aperture, also referred to as *conformal beam director*, which are composed of an array of small-size densely packed fiber collimators, as illustrated in Fig. 1(a) [1,2]. This interest is stimulated in part by an underlying presumption that the conformal beam directors can potentially replace conventional bulky and expensive optical transmitters based on large-aperture beam-forming telescopes. With a fiber-array laser transmitter, basic operation functions of laser beam projection systems such as beam pointing, target tracking, and adaptive mitigation of the propagation-medium-induced phase aberrations can potentially be directly integrated onto the fiber-collimator array and performed electronically [3].

In the conformal laser beam transmitter system in Fig. 1(a) the emitted outgoing laser beams (*beamlets*) are originated at the fiber tips located at fiber-collimator lens foci. The laser energy is delivered into these fiber tips from a multichannel master oscillator power amplifier (MOPA) system. The MOPA system is composed of an array of fiber amplifiers coupled to either a single seed laser as in Fig. 1(a) or to an array of independent laser sources [4,5].

In both fiber-array system types the optical path differences between the outgoing beamlets at the system output (pupil) plane are randomly changing, which leads to a corresponding random variation of the outgoing beamlet aperture-averaged phases, also known as *piston phases*, or phase shifts. Projection (focusing) of a conformal laser beam composed of an array of beamlets with random piston phases leads to their incoherent overlapping (combining) at the target plane—*target-plane incoherent beam combining* [6,7].

With optimal pointing of beamlets in vacuum resulting in their perfect overlapping, the characteristic size (diameter) b_T of the illuminated area at the target plane (*target hit-spot size*) depends inversely on the fiber-collimator aperture diameter d. Correspondingly, the major beam projection performance measure—power density inside the target hit-spot (*hit-spot brightness*)—is then proportional to the product $N_{sub}p_0d^2$ of the following three parameters: the number of fiber-array system subapertures N_{sub} (number of fiber collimators), the output power emitted through a single fiber collimator p_0 (power per fiber), and the subaperture diameter d. From this simplified consideration follows that the increase of the power density at the target plane desired in many applications is directly related to the increase of each of the above factors.

The increase in power-per-fiber parameter p_0 is typically limited by the nonlinear stimulated Brillion scattering (SBS) effect that accompanies high-energy laser beam propagation in a fiber [8] and the laser-induced damage threshold of fiber tips [9]. On the other hand, the increase of the number of subapertures N_{sub} and/or the fiber-collimator diameter d leads to a bulky transmitter aperture with limited capabilities for the outgoing conformal beam steering and pointing [10].

In principle, the target hit-spot power density can be increased using *pupil-plane incoherent beam combining* [4,5,11,12]. In this approach the outgoing beamlets are first combined into a single beam of diameter $d_c \sim d$, and the combined beam is then expanded to a larger beam of diameter $D \gg d_c$ using a conventional beam director system as shown in Fig. 1(b). The pupil-plane incoherent

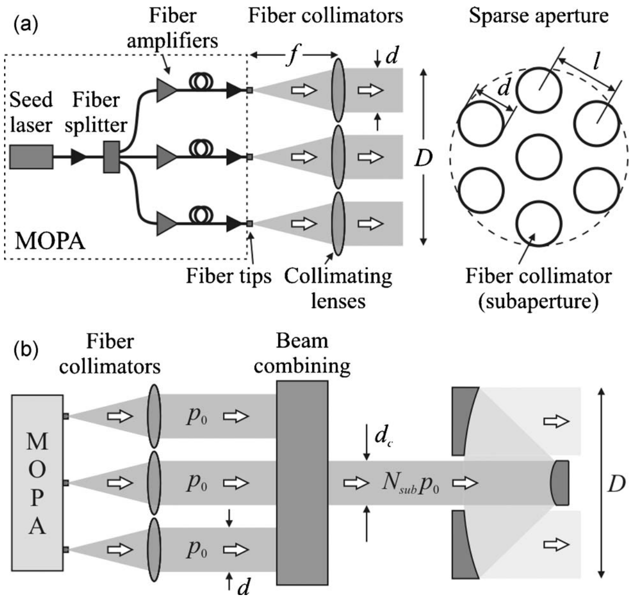

Fig. 1. Notional schematics of laser transmitter (beam director) based on (a) sparse (conformal) array of fiber collimators with a single laser source and (b) pupil-plane incoherent combining of laser beams originating from multiple laser sources.

beam combining can potentially lead to a target hit-spot brightness increase by a factor $(D/d)^2$. However, combining a large number N_{sub} of beamlets into a single beam presents a challenging technical task. Besides, this technique still requires a bulky (for large D) conventional beam-forming telescope.

In this study we consider an alternative approach in the development of the fiber-array-based laser beam projection systems known as a *coherent beam combining* [1,3,13–21]. In this approach the optical path differences between the beamlets transmitted by the fiber array are compensated (locked) either at the transmitter aperture (*pupil-plane coherent beam combining*) or at the target plane (*target-plane coherent beam combining*) or in both planes.

With ideal phase locking of densely packed beamlets in vacuum, one can potentially achieve beam projection performance comparable with the performance of a conventional beam director with a monolithic aperture of diameter D [19]. The corresponding aperture can be defined then by the smallest circle that contains all subapertures within it, as shown in Fig. 1(a) by the dashed curve.

Thus, phase locking of the outgoing beamlets (either pupil- or target-plane) allows potential achievement of $(D/d)^2$-fold increase of the target hit-spot brightness without increasing the number of fiber collimators N_{sub}, increasing the power p_0 transmitted through a single fiber-collimator, or a need to combine beamlets into a single beam with further aperture expansion. Note that with the currently available technologies, phase locking can be obtained only in fiber-array systems with a single seed laser [as in Fig. 1(a)] that has sufficiently narrow frequency bandwidth (typically on the order of a few megahertz or less [1,3]. In addition, the entire multichannel fiber system (MOPA system) should be able to support single-mode operation and provide identical polarization states for all output beamlets.

Note that a single narrow-line laser source and polarization-maintaining fiber requirements may no longer be limiting factors in the future. At a low power level, phase locking of an array of independent narrow-line laser sources has already been demonstrated [22,23]. Besides, recent progress in control of polarization states in fiber systems allows implementation of fiber-array systems with capabilities for locking of both phases and polarization states [24].

In this paper we consider the pupil-plane coherent beam combining achieved by locking of piston phases $\{\Delta_j(t)\}$, $j=1,\ldots,N_{sub}$, originated solely from laser beam propagation in a multichannel, single-mode polarization-maintained fiber system and inside the fiber collimators. The paper is organized as follows. Section 2 is dedicated to the review of conventional control techniques that are used for locking of piston phases in fiber-collimator array systems. A new type of piston phase-sensing method that uses interference of laser beam tails (two-beam-tail interference), as well as the corresponding different sensor network architectures, are introduced in Section 3. In this section we also analyze several phase-locking control algorithms and system architectures. In Section 4 the analysis of an array of interconnected feedback circuits is extended to include three-beam-tail sensors. Finally, in Section 5 we introduce the focal-plane beam-tail sensors and derive mathematical models of phase-locking control systems that account for the diffraction effects and finite size of sensors.

2. PUPIL-PLANE PHASE LOCKING: BASIC SYSTEM ARCHITECTURES

In the existing pupil-plane coherent beam-combining (phase-locking) systems, a small fraction $\kappa \ll 1$ of the outgoing conformal beam with the complex amplitude $A(\mathbf{r},t)$ is redirected into a phase-locking receiver using either a single beam splitter or an array of beam splitters that are located in front of the outgoing conformal beam, as illustrated in Fig. 2(a). Here $\mathbf{r}=\{x,y\}$ is the coordinate vector at both the transmitter aperture and the optical receiver input planes, and t is the time variable.

The major function of the phase-locking receiver is transformation of the outgoing conformal beam with the complex amplitude $\kappa A(\mathbf{r},t)$ into an output field $A_{out}(\mathbf{r},t)$ with the intensity distribution $I_{out}(\mathbf{r},t)=|A_{out}(\mathbf{r},t)|^2$ that depends on the piston phases of the outgoing beamlets.

The desired transformation is typically achieved by combining the outgoing beamlets either with a coherent reference field $A_{ref}(\mathbf{r})$, as in Fig. 2(b), or with each other. The latter arrangement can be easily obtained using a lens that focuses all the outgoing beamlets into the same area of the focal plane, as shown in Fig. 2(c). The overlapping of the beamlets results in their interference. The intensity distribution of the interference pattern $I_{out}(\mathbf{r},t)$—the receiver output—depends on the piston phases of the outgoing beamlets and hence can be utilized as an input signal for a phase-locking control system.

The feedback control loop in pupil-plane phase-locking systems can be either optical or electronic. In a phase-locking system with optical feedback, the output field $A_{out}(\mathbf{r},t)$ is coupled into a fiber tip that is located in the

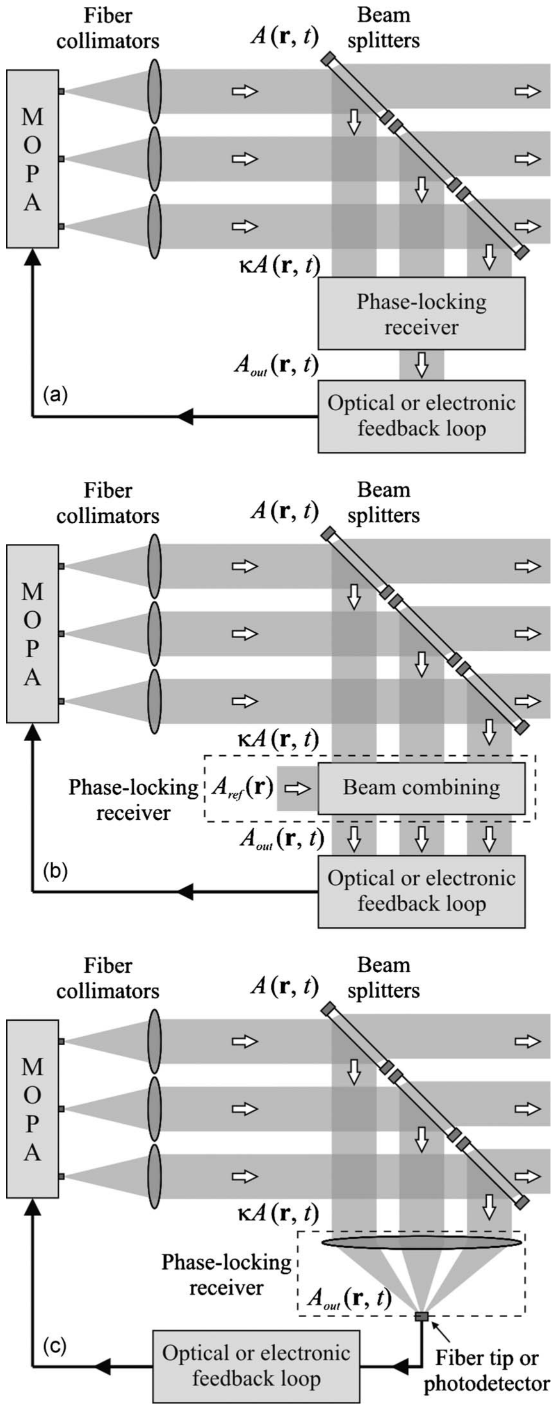

Fig. 2. Pupil-plane phase-locking control system basic architectures: (a) notional schematic, (b) phase-locking receiver system with a coherent reference wave, and (c) phase-locking receiver with focal-plane beam combining. The systems are based on either electronic or optical feedback loop.

focus of the combining beamlets' lens as shown in Fig. 2(c). The optical signal coupled into the fiber is further split and after amplification is combined with the laser beams entering the fiber amplifiers of the MOPA system, thus forming an array of mutually coupled nonlinear optical feedback circuits. As has been shown, nonlinear dynamics of these optical feedback circuits can lead to a self-organized stationary solution corresponding to a phase-locked state [25].

In another approach referred to as electronic phase-locking control, auxiliary controlling piston phase shifts $\{u_j(t)\}$, $j=1,\ldots,N_{sub}$, are injected into each beamlet by using, for example, phase-shifting elements integrated into the MOPA system. These phase shifts are used for compensation of the fiber-system-induced phase shifts $\{\Delta_j(t)\}$. With the injected controllable phase shifts $\{u_j(t)\}$, the piston phases of the outgoing beamlets $\{\delta_j(t)\}=\{\Delta_j(t)+u_j(t)\}$ correspond to uncompensated or residual piston phase errors, further also referred to as phase errors. Note that since piston phases of type $\{\delta_j(t)\pm 2\pi m\}$, where m is an arbitrary integer number, result in an identical optical field, the phase errors can be defined as modulo 2π functions, that is, $\{\delta_j(t)\}=\{\mathrm{mod}_{2\pi}[\Delta_j(t)+u_j(t)]\}$.

The phase-locking receiver output field is registered by either a single photodetector or an array of $1<M\leqslant N_{sub}$ photodetectors—a part of the feedback loop. The obtained electronic signals (metrics) $\{J_l(t)\}$, $l=1,\ldots,M$, depend on the uncompensated phase shifts $\{\delta_j(t)\}$. These signals are sent to an electronic processor (phase-locking feedback controller) that forms control signals applied to the phase-shifting elements—typically the lithium niobate ($LiNbO_3$) electro-optics phase modulators integrated into each channel of the MOPA system [24,26,27].

Compensation of the residual phases (pupil-plane phase locking) is commonly based on control techniques widely used in active interferometers (laser vibrometers) and adaptive optics, namely, the optical path difference stabilization, also known as heterodyne, and metric optimization techniques. In its turn, the metric optimization is performed using either multidithering [28] (also recently referred to as LOCSET [29]) or the stochastic parallel gradient descent (SPGD) control techniques [3,30,31].

In the heterodyne phase-locking systems the outgoing beamlets are optically combined with a reference optical wave (see, e.g., [17]). An optical beam originated from the same MOPA system is commonly used as a reference. The entire control system consists then of N_{sub} independent interferometers, as shown in Fig. 3(a).

The output field of each interferometer enters a diaphragm (pinhole) with a single photodetector located immediately behind it. The pinhole size does not exceed the characteristic size of the interference fringes which is dependent on accuracy of angular alignment of the reference wave and beamlets.

The output signal $J_j[\delta_j(t)]$ measured by the photodetector at the jth control channel depends solely on the phase error $\delta_j(t)$. Correspondingly, the phase-locking controller is composed of an array of N_{sub} independently operating identical control subsystems used for active stabilization of the interference patterns.

The interference signal $J_j[\delta_j(t)]$ can be represented as the sum of two components: $J_j[\delta_j(t)]=J_j^0(t)+\tilde{J}_j(t)$, where $J_j^0(t)$ is the independent-of-phase-error signal (dc component), and $\tilde{J}_j(t)=\eta_j\cos\delta_j(t)$ is the interference term. The coefficient $0<\eta_j\leqslant 1$ is associated with interference pattern visibility. Electronic signal processing of the regis-

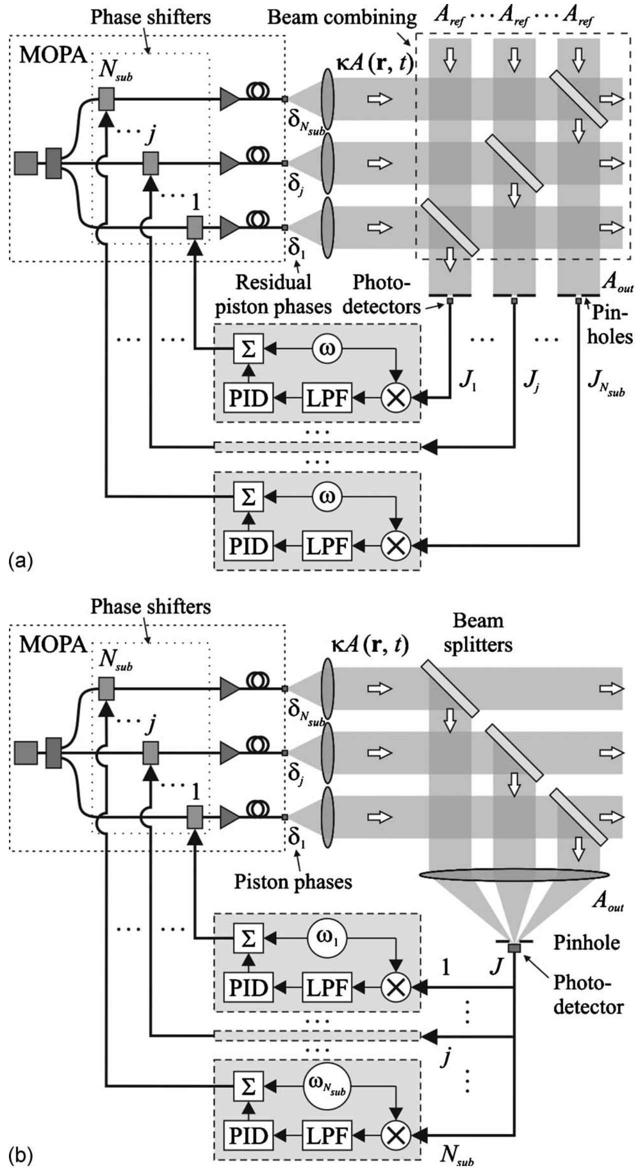

Fig. 3. Principal schematics of pupil-plane phase-locking optical systems based on optical path difference stabilization with (a) heterodyne signal detection and (b) multidithering control techniques. Here ω, Σ, LPF, and PID denote, respectively, dither signal generation, signal summation, low-pass electrical filtering, and proportional-integral-derivative control.

tered signal in each control channel aims at the extraction of the solely interference component $\tilde{J}_j(t)$ (or its derivative) that is used for compensation of the phase error.

The components $\{\tilde{J}_j(t)\}$ can be obtained by injecting a small-amplitude sinusoidal signal (dither) with frequency ω into either the reference wave or into outgoing beamlets. In the latter case the dither signal is superimposed with the control signal applied to the corresponding phase-shifting element of the MOPA system as shown in Fig. 3(a). Using a standard synchronous detection technique, the signals $\{\tilde{J}_j(t)\}$ (or their derivatives) can be electronically separated. The electronic signal processing includes multiplication of the measured $\{J_j\}$ and dither signals. The signal components $\{\tilde{J}_j(t)\}$ are then separated by low-pass filtering (LPF) of the product, as shown in Fig. 3(a). The obtained signals enter the proportional-integral-derivative (PID) controllers [32]. The dynamic processes in the PID control system ideally lead to stationary steady states of type $\delta_j(t\rightarrow\infty)=\text{const}+2\pi m_j$, where $j=1,\ldots,N_{sub}$ and $\{m_j\}$ are integers, which correspond to locking of the outgoing-beamlet piston phases.

The major drawback of the phase-locking technique based on optical path difference stabilization is related to technical difficulties in the design and alignment of the phase-locking receiver system composed of an array of laser interferometers. Such an optical system is quite sensitive to various distortions including vibrations, thermal effects, and acoustical waves that may lead to parasitic phase shifts that affect phase-locking system performance.

These problems can be overcome in the self-reference-type phase-locking receiver shown in Figs. 2(c) and 3(b). In this system the lens focuses beamlets into a joint focal-plane area where all of them overlap, forming an intensity pattern that depends on all uncompensated piston phases [residual phase shifts $\{\delta_j(t)\}$].

For this receiver system, maximization of the on-axis focal-plane intensity value leads to ideal phase locking. Thus, the signal J obtained by measuring the light power inside a small pinhole located in the lens focus can be used as a measure (metric) of phase-locking system performance. The measured metric signal $J[\delta_1(t),\ldots,\delta_j(t),\ldots,\delta_{N_{sub}}(t)]$ is a function of all phase errors. Note that this function has an infinite number of identical global maxima corresponding to phase errors whose values differ by 2π multiplied by an arbitrary integer number. Phase locking can then be considered as a process of metric J maximization performed using one or another optimization technique known in adaptive optics (multidithering, gradient descent, SPGD, etc.).

As an example, consider the phase-locking controller based on the multidithering technique, as shown in Fig. 3(b). Each channel of this control system is similar to the heterodyne phase-locking controller in Fig. 3(a). The important difference is that small perturbations of phase shifts (dithering signals) $a\sin(\omega_j t)$ in this system have different frequencies ω_j, where a is the dither amplitude and $j=1,\ldots,N_{sub}$. Input signal (metric J) is multiplied in each control channel by the corresponding dither signal. The low-pass filtering of the products allows extraction of the gradient projections $\{J'_j\}=\{\partial J/\partial u_j\}$ of the metric J. The obtained metric gradient components $\{J'_j\}$ are used as the error signals in the continuous-time gradient descent controller [33]:

$$\tau\frac{\mathrm{d}u_j(t)}{\mathrm{d}t}=\gamma_j J'_j[\delta_1(t),\ldots,\delta_j(t),\ldots,\delta_{N_{sub}}(t)]$$

$$(j=1,\ldots,N_{sub}). \tag{1}$$

Here τ is the characteristic response time of the control system and $\{\gamma_j\}$ are the feedback gain coefficients. The dynamical process (1) leads to optimization of the metric signal (maximization of the power inside a pinhole) and, correspondingly, locking of the piston phases. The control method associated with the dynamical process (1) is also known as the gradient-flow optimization technique [34,35].

Consider briefly a phase-locking system based on SPGD feedback control [3,30]. Note that the phase-locking receivers in the SPGD and multidithering systems are identical, while the operation principle is quite different. In the SPGD control system, optimization of metric J is performed using an iterative process. At each nth iteration of this process the controllable piston phases of the outgoing beamlets $\{u_j^{(n)}\}$ are simultaneously perturbed using a set of small-amplitude random phase shifts (perturbations) $\{\Delta u_j^{(n)}\}$. The perturbation of the piston phases results in the corresponding variation $\Delta J^{(n)}$ of the measured metric signal. The piston phases at the $(n+1)$th iteration, $\{u_j^{(n+1)}\}$, are then computed using the following simple rule [30]:

$$u_j^{(n+1)} = u_j^{(n)} + \gamma^{(n)}\Delta J^{(n)}\Delta u_j^{(n)} \qquad (j=1,\ldots,N_{sub}), \qquad (2)$$

where $\gamma^{(n)}$ is the gain coefficient at the nth iteration. It can be shown that with an appropriate choice of the perturbation amplitudes and gain coefficients, the iterative process (2) leads to metric J maximization [31].

Both multidithering and SPGD techniques require fast (high operational frequency bandwidth) phase-shifting elements. In the multidithering phase-locking systems, high-frequency bandwidth of phase-shifting elements is required for obtaining sufficiently wide separation between the dithering frequencies $\{\omega_j\}$, which is necessary for prevention of strong cross-coupling between the control channels leading to a decrease in signal-to-noise ratio in the gradient projection measurements [28].

In its turn in the SPGD phase-locking technique, the fast operational speed of phase-shifting elements allows a high iteration rate and, correspondingly, an increase in the control system bandwidth. Fortunately, the existing fiber-integrated phase-shifting elements are sufficiently fast ($>$ MHz bandwidth) and hence can provide efficient compensation of relatively slowly varying phase shifts $\{\Delta_j(t)\}$ (typically on the order of 10^1-10^3 Hz) that are caused by temperature fluctuations and/or vibrations and mechanical deformation of fiber elements in the MOPA system.

Perhaps the most serious drawback of the existing pupil-plane phase-locking systems is the presence of a beam splitter (or a beam splitter array) located in front of the outgoing conformal beam, as shown in Figs. 2 and 3. This beam splitter is part of the phase-locking receiver system used for sampling of piston phases of the outgoing beamlets. For large-aperture fiber-array beam directors, this receiver system type is quite difficult to implement in practice since the diameter of a monolithic beam splitter should exceed the overall diameter D of the entire fiber array that would require the use of a bulky and expensive optical element. Such a beam splitter also causes a lateral shift of the conformal laser beam and can potentially result in additional phase aberrations, especially for high-power systems.

The replacement of a monolithic beam splitter with a beam splitter array does not solve the problem since each element of this array needs to be mounted onto a separate holder with tip–tilt alignment capabilities. This makes the dense packaging of these beam splitting elements required for high-fill-factor fiber-array systems difficult.

3. OBSCURATION-FREE PHASE LOCKING WITH TWO-TAIL SENSORS

A. Piston Phase Sensing Based on Interference of Two Beam Tails

In this paper we introduce another approach for sampling of piston phases that does not require splitting of the outgoing conformal beam with a pupil-plane beam splitter. First, note that each lens in the fiber-collimator array in Fig. 1(b) clips a central region of the beam exiting the corresponding fiber tip. The optical field energy located in the tail region of this beam (on the order of 8%–10% of the transmitted laser beam energy [3,19]) is absorbed by optical and mechanical elements of the fiber-collimator array and commonly results in undesirable phase aberrations caused by the heat-induced thermal deformation of optical and mechanical elements and air convection inside the fiber collimators. In this section we show that the optical field belonging to these beam-tail regions can be utilized for sensing of piston phases of the outgoing beamlets.

To illustrate the basic principle of piston phase sensing using truncated (tail) regions of the beams generated inside the fiber-collimator array, consider two neighboring fiber collimators that are denoted as A_1 and A_2 in Fig. 4(a). The tail regions of the corresponding beams overlap inside a volume region Ω. This overlapping leads to interference of the corresponding optical fields, which is referred to here as two-beam-tail or just two-tail interference, to be short.

Consider a plane inside Ω, which is orthogonal to the direction *oz* of laser beam propagation (direction of the optical axis) and located a distance f_0 from the fiber tips (or a distance $l_0=f-f_0$ from the fiber-array pupil plane). The intensity distribution in this plane depends on the phase errors $\delta_1(t)$ and $\delta_2(t)$ of the interfering beam tails as well as on the fiber-array characteristics such as beam divergence, propagation distance f_0, and the offset distance l between the neighboring fiber collimators.

Consider a small-size photodetector at the selected plane S inside Ω, as shown in Fig. 4(a). We assume that the photodetector size does not exceed the characteristic width w of interference fringes (point-size photodetector). The signal (metric) $J_{1,2}(t)$ registered by the photodetector is then given by

$$\begin{aligned} J_{1,2}(t) &= J_{1,2}[\delta_1(t),\delta_2(t)] \\ &= I_1 + I_2 + 2\sqrt{I_1 I_2}\cos[\delta_2(t)-\delta_1(t)+\zeta_{1,2}], \end{aligned} \qquad (3)$$

where I_1 and I_2 are the intensity values of optical fields corresponding to the fiber collimators A_1 and A_2 at the photodetector, and $\zeta_{1,2}$ is the static phase term dependent on the photodetector position at the registration plane. Thus, the difference between the piston phases of two neighboring subapertures can be sensed using a single photodetector located in the area of beam-tail overlapping. We assume for simplicity that the photodetector can be placed at a point corresponding to $\zeta_{1,2}=2\pi m$, where m

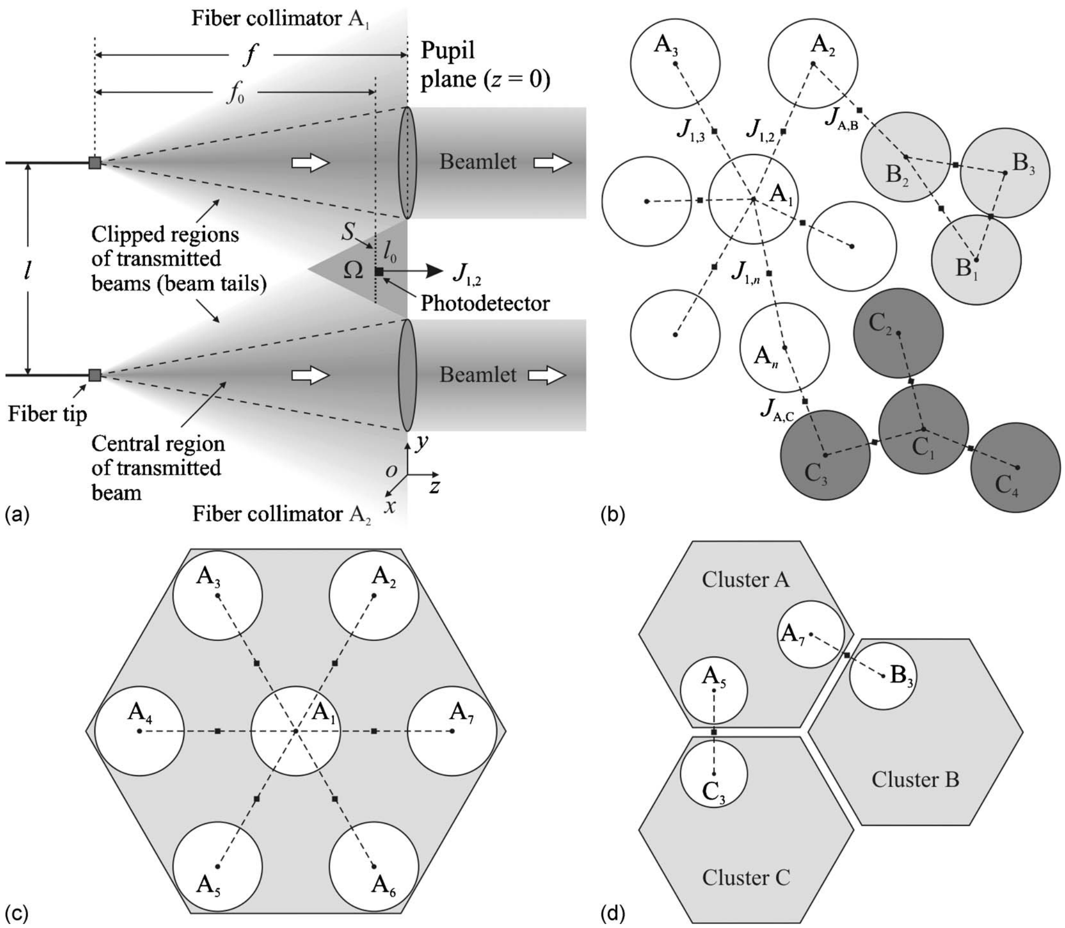

Fig. 4. Sensing of piston phases using interference of tail sections of two beamlets in fiber-collimator array systems: (a) schematic illustration of two-tail interference, (b) fiber-array system composed of three clusters (A, B, and C) coupled by two-tail sensors, (c) two-tail sensing of piston phases in a cluster A composed of seven fiber collimators with hexagonal arrangement, and (d) coupling of three hexagonal clusters using two-tail interference sensors. Black squares in (b)–(d) denote point-size photodetectors.

is an arbitrary integer number, so we can omit $\zeta_{1,2}$ thereafter.

The major advantage of the described sensing technique, referred to here as obscuration-free piston phase sensing, is the absence of a beam splitter. Sensing of piston phases is obtained here without any additional optical element by simply installing a set of photodetectors that are located outside the outgoing beamlets.

B. Fiber-Array Cluster

Consider now the subaperture A_1 as a reference and select a set of N_0-1 neighboring the reference subapertures $A_2,\ldots,A_j,\ldots,A_{N_0}$, where $N_0\leqslant N_{sub}$, as shown in Fig. 4(b). The reference and the neighboring fiber collimators (subapertures) are referred to here as a *cluster* (cluster A). Assume that a set of point-size photodetectors are located inside the overlapping regions of the beam tails corresponding to the reference and neighboring subapertures of the cluster, as illustrated in Fig. 4(b). For the considered case of two-tail sensing, the number of photodetectors M coincides with the number of neighboring subapertures N_0-1. Analogously to expression (3), the metric registered by the jth photodetector,

$$J_{1,j}(t)=J_{1,j}[\delta_1(t),\delta_j(t)]=I_1+I_j+2\sqrt{I_1I_j}\cos[\delta_j(t)-\delta_1(t)]$$

$$(j=2,\ldots,N_0), \tag{4}$$

depends solely on the differences $\delta_j(t)-\delta_1(t)$ between the piston phases $\delta_j(t)$ and $\delta_1(t)$. In Eq. (4), I_j describes the intensity of the optical field component associated with the jth subaperture. For simplicity we ignore here the contributions to the metric signal $J_{1,j}(t)$ from the beam tails belonging to remote subapertures, assuming that these contributions are sufficiently small due to a sharp drop in the intensity of the Gaussian beam with the distance.

C. Phase Locking of a Fiber-Array Cluster via Gradient-Flow Control

Consider the fiber-array cluster A in Fig. 4(b). Within this cluster, the optical field belonging to the beam tail of the fiber collimator A_1 plays the same role as the reference field in the phase-locking system based on the interferometric (heterodyne) type receiver discussed in Section 2 and shown in Figs. 2(b) and 3(a). Correspondingly, phase locking of the fiber collimators belonging to the fiber-array cluster can be performed using the heterodyne technique described above. As already mentioned in Section 2, this control strategy is equivalent to the continuous-time gradient descent or the gradient-flow optimization (control) of the measured signals $\{J_{1,j}(\delta_1,\delta_j)\}$ (local metrics) corresponding to neighboring subapertures.

With this control technique, the dynamics of the phase-locking process inside a single cluster can be described by the following set of equations:

$$\tau\frac{\mathrm{d}\delta_j(t)}{\mathrm{d}t}=\gamma_j J'_{1,j}[\delta_1(t),\delta_j(t)] \qquad (j=2,\ldots,N_0), \tag{5}$$

where $J'_{1,j}[\delta_1(t),\delta_j(t)]=\sin[\delta_1(t)-\delta_j(t)]=\sin[\Delta_1+u_1(t)-\Delta_j-u_j(t)]$ are the derivatives (gradient components) of the local metric signals (4) over the phase errors $\{\delta_j(t)\}$, and $\{\gamma_j\}$ are the feedback gain coefficients. Note that since the beam tail of the fiber collimator A_1 is used as a reference, the phase $u_1(t)$ does not have an impact on the phase-locking dynamics of the cluster and hence can be arbitrarily chosen, e.g., set to zero. In Eqs. (5) we assumed that during the transition (phase-locking) process with the characteristic control system response time τ, the phases $\{\Delta_j(t)\}$ can be considered stationary, that is, $\Delta_j(t)=\Delta_j$ for all $j=1,\ldots,N_0$.

The signals $J'_{1,j}=\sin[\Delta_1-\Delta_j-u_j(t)]$ in Eqs. (5) can be obtained using heterodyne-based synchronous detection signal processing, as in Fig. 3(a). It can be easily shown that a steady-state solution of the system of equations (5) can be represented in the form $\{\delta_j(t\to\infty)\}=\mathrm{mod}_{2\pi}(\delta_1)=\mathrm{mod}_{2\pi}(\Delta_1)$ that corresponds to the phase-locked state.

As an example of the phase-locking-process dynamics, consider a fiber-array cluster composed of seven fiber collimators with hexagonal arrangement as shown in Fig. 4(c). Equations (5) are numerically integrated over a time interval $T=10\tau$ using the fourth-order Runge–Kutta method [36]. The initial values of the phase errors are assumed to be random with uniform probability distribution within the interval $[-\pi,\pi]$. An example of temporal evolution of phase errors $\delta_j(t)$, $j=1,\ldots,7$, is shown in Fig. 5(a). Phase locking here corresponds to the transitioning to the steady-state solution $\delta_j(t\to\infty)=\delta_1$ occurring during the time interval $T\sim 5\tau$. Note that with the increase of the initial phase error amplitudes, the transitioning to the stationary steady state is commonly accompanied by 2π jumps in phase error values. In Fig. 5 these 2π phase jumps are removed.

As a phase-locking performance metric, consider the ensemble-averaged sum of squared phase error deviations from the reference phase $\delta_1=\Delta_1=\mathrm{const}$,

$$\sigma_\delta^2(t)=\left\langle \frac{1}{N_0-1}\sum_{j=2}^{N_0=7}[\delta_j(t)-\delta_1]^2\right\rangle. \tag{6}$$

The ensemble averaging, denoted by the angular brackets in Eq. (6), is performed over 1000 random realizations of initial phase shifts. The results of numerical simulations are presented in Fig. 5(b) as time dependence of the standard deviation $\sigma_\delta(t)$. As can be seen, phase-locking control results in nearly 10^2-fold decrease of σ_δ during time interval $T\sim 8\tau$.

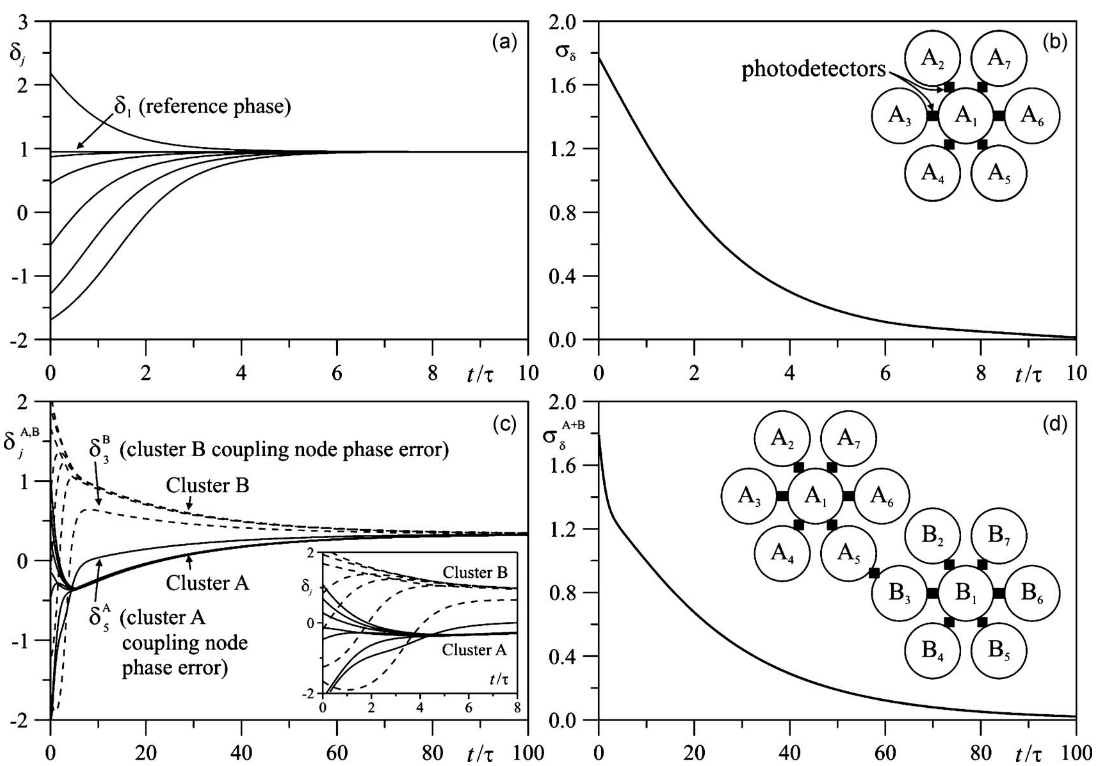

Fig. 5. Phase locking based on the gradient-flow optimization control in a fiber-array system with two-tail sensors for (a), (b) a single cluster and (c), (d) two coupled clusters shown in the top-right inserts in (b) and (d). Temporal dynamics of phase errors $\{\delta_j(t)\}$ from random initial conditions $\{\delta_j(0)\}$ in (a) and (c) and the ensemble-averaged phase-locking error standard deviations $\sigma_\delta(t)$ and $\sigma_\delta^{A+B}(t)$ in (b) and (d) are obtained by numerical integration of Eqs. (5) with $\gamma_j=1$, $j=2,\ldots,7$, and Eqs. (7) and (8) with $\gamma_j^{A}=\gamma_j^{B}=1$, $j=1,\ldots,7$, and $\gamma_{A,B}=\gamma_{B,A}=0.5$, respectively. The reference phase δ_1 is shown by the horizontal line in (a). The insert in (c) illustrates an initial stage of the phase-locking process.

D. Coupled Fiber-Array Clusters

Consider now phase locking of a fiber-array system composed of a set of clusters. As an example, a fiber-array system containing three mutually coupled clusters (denoted as A, B, and C) is shown in Fig. 4(b). The question to ask is how can these clusters be locked together?

Note that phase locking of different clusters requires sensing of phase errors for beamlets belonging to different clusters. This can be achieved using beam tails belonging to different clusters, shown in Fig. 4(b). The photodetectors and the corresponding metric signals (such as metrics $J_{\mathrm{A,B}}$ and $J_{\mathrm{A,C}}$) that are used for inter-cluster coupling define the coupling node. For example, in Fig. 4(b), intercoupling of clusters A and B is achieved using the subapertures A_2 and B_2, while clusters A and C are connected through the subapertures A_n and C_3. Note that the same clusters can be connected using several coupling nodes. At the same time, phase locking of the entire fiber array does not require a direct connection between all clusters in the array. For example, in Fig. 4(b), clusters B and C are not directly coupled (although this coupling can be introduced, e.g., by using the subapertures C_2 and B_1). Coupling between those clusters is achieved indirectly using the sensing nodes coupling these two clusters with the cluster A.

E. Dynamics of Coupled Fiber-Array Clusters

The mathematical model describing the phase-locking process in a fiber-array system composed of several coupled clusters (cluster network) can be obtained by introducing the following changes to the system of equations (5). First, the mathematical model for the cluster network should include additional equations describing dynamics of phase errors corresponding to the reference beams. In Fig. 4(b) these are the phase errors corresponding to fiber collimators A_1, B_1, and C_1. Second, the equations for coupling nodes in each cluster should include additional terms that depend on the inter-cluster metrics [such as, for example, metrics $J_{\mathrm{A,B}}$ and $J_{\mathrm{A,C}}$ in Fig. 4(b)].

For the sake of simplicity, consider the system with only two clusters (A and B) composed of N_0^{A} and N_0^{B} fiber collimators, respectively. Assume that each cluster has a single coupling node: one corresponding to the subaperture i (cluster A) and another to the subaperture k (cluster B). With the introduced notation, the mathematical model describing the phase-locking process in this system can be represented in the following form:

$$\tau\frac{\mathrm{d}\delta_j^{\mathrm{A}}(t)}{\mathrm{d}t} = \gamma_j^{\mathrm{A}}\sin[\delta_1^{\mathrm{A}}(t)-\delta_j^{\mathrm{A}}(t)] + \kappa_{ji}\gamma_{\mathrm{A,B}}\sin[\delta_k^{\mathrm{B}}(t)-\delta_j^{\mathrm{A}}(t)]$$

$$(j=2,\ldots,N_0^{\mathrm{A}}), \tag{7a}$$

$$\tau\frac{\mathrm{d}\delta_1^{\mathrm{A}}(t)}{\mathrm{d}t} = -\frac{1}{N_0^{\mathrm{A}}-1}\sum_{j=2}^{N_0^{\mathrm{A}}}\gamma_j^{\mathrm{A}}\sin[\delta_1^{\mathrm{A}}(t)-\delta_j^{\mathrm{A}}(t)], \tag{7b}$$

$$\tau\frac{\mathrm{d}\delta_j^{\mathrm{B}}(t)}{\mathrm{d}t} = \gamma_j^{\mathrm{B}}\sin[\delta_1^{\mathrm{B}}(t)-\delta_j^{\mathrm{B}}(t)] + \kappa_{jk}\gamma_{\mathrm{B,A}}\sin[\delta_i^{\mathrm{A}}(t)-\delta_j^{\mathrm{B}}(t)]$$

$$(j=2,\ldots,N_0^{\mathrm{B}}), \tag{8a}$$

$$\tau\frac{\mathrm{d}\delta_1^{\mathrm{B}}(t)}{\mathrm{d}t} = -\frac{1}{N_0^{\mathrm{B}}-1}\sum_{j=2}^{N_0^{\mathrm{B}}}\kappa_j^{\mathrm{B}}\sin[\delta_1^{\mathrm{B}}(t)-\delta_j^{\mathrm{B}}(t)]. \tag{8b}$$

Here $\kappa_{ji}=1$ for $i=j$ and zero otherwise, and $\delta_j^{\mathrm{A,B}}(t)$ and $\gamma_j^{\mathrm{A,B}}$ are, respectively, the phase errors and the gain coefficients for either the A or the B cluster. The coefficients $\gamma_{\mathrm{A,B}}$ and $\gamma_{\mathrm{B,A}}$ in Eqs. (7a) and (8a) describe the inter-cluster coupling strength. The dynamics of phase errors in cluster A is described by Eqs. (7) and in cluster B by Eqs. (8). Equations (7b) and (8b) correspond to the phases of the reference beamlets.

It is easy to show that the system of equations (7) and (8) has the following stable steady-state solutions:

$$\delta_j^{\mathrm{A}}(t\to\infty) = \mathrm{mod}_{2\pi}[\delta_1^{\mathrm{A}}(t\to\infty)]\ (j=2,\ldots,N_0^{\mathrm{A}}), \tag{9a}$$

$$\delta_j^{\mathrm{B}}(t\to\infty) = \mathrm{mod}_{2\pi}[\delta_1^{\mathrm{B}}(t\to\infty)]\ (j=2,\ldots,N_0^{\mathrm{B}}), \tag{9b}$$

$$\delta_1^{\mathrm{A}}(t\to\infty) = \mathrm{mod}_{2\pi}[\delta_1^{\mathrm{B}}(t\to\infty)]. \tag{9c}$$

These solutions correspond to locking of phases both inside each cluster [Eqs. (9a) and (9b)] and between the clusters [Eq. (9c)].

Consider first weak inter-cluster coupling and assume that in Eqs. (7) and (8) $\gamma_j^{\mathrm{A}}=\gamma_j^{\mathrm{B}}=\gamma_j$ and $\gamma_{\mathrm{A,B}}=\gamma_{\mathrm{B,A}}\ll\gamma_j$. In this case, the dynamics of phase errors can be described as a two-stage evolution process. The first stage is characterized by a relatively fast locking of phases within each cluster. This process occurs during the time interval $0<t<t_1$. At the end of this stage the piston phases are nearly locked within each cluster, so that $\delta_j^{\mathrm{A}}(t_1)\cong\mathrm{mod}_{2\pi}[\delta_1^{\mathrm{A}}(t_1)]$ and $\delta_j^{\mathrm{B}}(t_1)\cong\mathrm{mod}_{2\pi}[\delta_1^{\mathrm{B}}(t_1)]$. Correspondingly, the system of equations (7) and (8) can then be reduced to the following two equations describing the second stage of the phase-locking process—a relatively slow decrease of the phase difference between two clusters:

$$\tau\frac{\mathrm{d}\delta_i^{\mathrm{A}}(t)}{\mathrm{d}t} = \gamma_{\mathrm{A,B}}\sin[\delta_k^{\mathrm{B}}(t)-\delta_i^{\mathrm{A}}(t)], \tag{10a}$$

$$\tau\frac{\mathrm{d}\delta_k^{\mathrm{B}}(t)}{\mathrm{d}t} = \gamma_{\mathrm{A,B}}\sin[\delta_i^{\mathrm{A}}(t)-\delta_k^{\mathrm{B}}(t)]. \tag{10b}$$

This inter-cluster phase locking occurs with a characteristic time that is significantly longer, on the order of $\gamma_{\mathrm{A,B}}/\gamma_j\ll 1$.

An example of the phase-locking dynamics in the system with two clusters composed of $N_0^{\mathrm{A}}=N_0^{\mathrm{B}}=7$ fiber collimators is illustrated in Figs. 5(c) and 5(d). The geometry of the system is shown by the insert in Fig. 5(d). The clusters are coupled through a single node (subapertures A_5 and B_3) with the gain and coupling coefficients $\gamma_j^{\mathrm{A}}=\gamma_j^{\mathrm{B}}=\gamma$, $j=1,\ldots,7$, $\gamma_{\mathrm{AB}}=\gamma_{\mathrm{BA}}=\gamma_c$, and $\gamma_c/\gamma=0.5$. As can be seen from Fig. 5(c), the in-cluster phase locking nearly ends at $T\sim 6\tau$ (see the insert), while the inter-cluster phase locking occurs over a significantly longer time, $T\sim 100\tau$.

Time dependence of the ensemble-averaged phase error metric $\sigma_\delta^{\mathrm{A+B}}(t)$ that is described by an expression similar to Eq. (6) but includes all 14 participating subapertures is shown in Fig. 5(d). An initial sharp decrease in the phase error metric $\sigma_\delta^{A+B}(t)$ at $t \sim 4\tau$ is associated with the in-cluster phase locking—the first stage of the system dynamics described above. The numerical simulations show that with an increase of the ratio γ_c/γ up to unity, both in- and inter-cluster phase locking occur on nearly the same time scale, which corresponds to the optimal scenario, while a further increase of the ratio γ_c/γ leads to a relatively weaker in-cluster coupling and the corresponding slowdown of the overall phase-locking dynamics.

F. Phase Locking via SPGD Optimization

The obscuration-free pupil-plane phase locking can also be achieved using direct optimization of measured signals (metrics), as described in Section 2. In this control approach, signals from a set of photodetectors can be used as local metrics, or, alternatively, these metrics can be electronically combined into a single phase-locking performance metric.

To illustrate, consider a signal (local metric) $J_{l,k}[\delta_l(t),\delta_k(t)]$ measured with a two-tail interference sensor coupling two neighboring subapertures l and k. Similarly to Eq. (4), for the local metric we have

$$J_{l,k}(t) = J_{l,k}[\delta_l(t),\delta_k(t)] = I_l + I_k + 2\sqrt{I_l I_k}\cos[\delta_k(t) - \delta_l(t)]$$

$$(k = 1, \ldots, N_0;\ k \neq l). \tag{11}$$

Assume that a metric $J_\Sigma(t)$ (global or combined metric) is obtained by electronically combining M local metrics,

$$J_\Sigma(t) = \sum_{k>l}^{M} J_{l,k}[\delta_l(t),\delta_k(t)]. \tag{12}$$

The set of sensors and the corresponding signals (local metrics) that are included in the sum (12) can be different, but optimization of the combined metric $J_\Sigma(t)$ can lead to the phase-locked state only if this metric depends on the phase errors of the entire fiber-array system: $J_\Sigma = J_\Sigma[\delta_1(t), \ldots, \delta_{N_{sub}}(t)]$.

The phase locking based on the SPGD control can be performed using optimization of either local metrics $J_{l,k}$ or the combined metric J_Σ. Similarly to Eq. (2), one can easily derive the corresponding SPGD control update equations for both phase-locking system types. In the case of the combined metric we have

$$\delta_j^{(n+1)} = \delta_j^{(n)} + \gamma_\Sigma^{(n)} \Delta J_\Sigma^{(n)} \Delta\delta_j^{(n)} \quad (j = 2, \ldots, N_0;\ n = 1, \ldots), \tag{13}$$

where $\Delta J_\Sigma^{(n)}$ is the metric perturbation in response to control signal perturbations $\{\Delta\delta_j^{(n)}\}$, and $\gamma_\Sigma^{(n)}$ is the gain coefficient at the nth iteration. Note that the subaperture $j=1$ is considered here as a reference.

For the phase-locking control system based on SPGD optimization of the local metrics we have

$$\delta_j^{(n+1)} = \delta_j^{(n)} + \gamma_j^{(n)} \Delta J_{1,j}^{(n)} \Delta\delta_j^{(n)} \quad (j = 2, \ldots, N_0; \quad n = 1, \ldots), \tag{14}$$

where $\{\Delta J_{1,j}^{(n)}\}$ and $\{\gamma_j^{(n)}\}$ are, respectively, the local metric perturbations and the gain coefficients at the nth iteration. The control rule (14) describes a set of weakly coupled identical SPGD optimization processes operating in parallel. Note that the control loops in Eq. (14) are coupled only through a piston phase corresponding to a reference subaperture ($j=1$). This control algorithm represents a clone of the SPGD optimization algorithm known as the decoupled SPGD (D-SPGD) control [37].

As an example of phase-locking control based on SPGD and D-SPGD optimization approaches, consider the fiber-array configurations composed of a single cluster as in Fig. 4(c). The numerical simulations results are presented in Fig. 6. Evolution of the phase errors during the SPGD and D-SPGD iteration processes (13) and (14) with identical random initial conditions $\{\delta_j(t=0)\} = \{\delta_j^{(0)}\}$ for both cases are shown in Figs. 6(a) and 6(b), respectively. The phase-locking process convergence occurs significantly faster (approximately eight-fold) with parallel optimization of the local metrics using D-SPGD controller (14). A similar conclusion can be made based on analysis of the normalized ensemble-averaged phase-locking performance measures $\langle \hat{J}_\Sigma(t)\rangle \equiv \langle J_\Sigma(t)\rangle / J_\Sigma^0$ and $\sigma_\delta(t)$ in Figs. 6(c) and 6(d), where J_Σ^0 is the combined metric corresponding to zero phase errors. Numerical analysis of the phase-locking process in the fiber-array system composed of two clusters as in Fig. 5(d) also demonstrated significantly faster convergence in the case of parallel optimization of the local metrics [D-SPGD controller similar to Eq. (14)].

4. PUPIL-PLANE PHASE LOCKING WITH THREE-TAIL SENSORS

A. Piston Phase Sensing Based on Interference of Three Beam Tails

Piston phase sensing based on the two-tail interference technique requires at least $N_{sub}-1$ sensors. For a fiber array with a large number of fiber collimators N_{sub}, the corresponding sensor network can be quite complicated.

The number of sensors can be significantly reduced using the three-tail interference sensing technique described in this section. In this approach, photodetectors are placed in the overlapping region of beam tails belonging to three neighboring subapertures, as shown in the insert in Fig. 7(a). Note that sensing of piston phases in the array of seven fiber collimators in this figure requires three photodetectors [small gray circles in the insert in Fig. 7(a)] for the three-tail and six photodetectors [black squares in the insert in Fig. 5(b)] for the two-tail interference technique. In addition, as can be seen from these figures, the physical space available for the photodetectors is sufficiently larger in the three-tail interference sensing technique.

To obtain an analytical expression for the signal (metric) registered by a three-tail interference sensor, consider the neighboring subapertures A_l, A_k, and A_m and a point-size photodetector located inside the overlapping region of the corresponding beam tails. Similarly to expression (3), the metric signal (with accuracy to a constant multiplier and a phase shift dependent on the photodetector position) is given by

$$\begin{aligned} J_{l,k,m}(t) &= J_{l,k,m}[\delta_l(t),\delta_k(t),\delta_m(t)] \\ &= |I_l^{1/2}\exp[i\delta_l(t)] + I_k^{1/2}\exp[i\delta_k(t)] \\ &\quad + I_m^{1/2}\exp[i\delta_m(t)]|^2, \end{aligned} \tag{15}$$

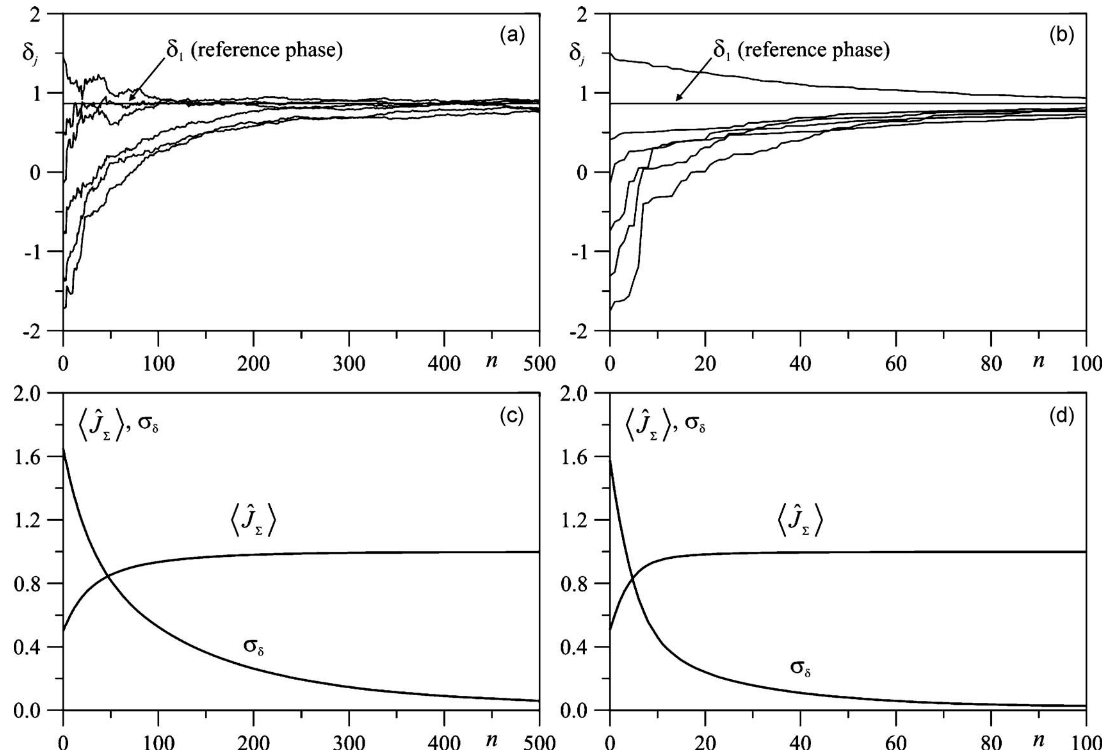

Fig. 6. Pupil-plane phase locking of the fiber-array cluster system as in Fig. 4(c) with two-tail sensors using optimization of (a), (c) the combined and (b), (d) the local metrics. Dynamics of the residual piston phase errors $\{\delta_j(t)\}$, $j=1,\ldots,7$, from an identical set of random initial conditions in (a) and (b) and the ensemble-averaged phase-locking performance metrics $\langle \hat{J}_\Sigma(t)\rangle$ and $\sigma_\delta(t)$ in (c) and (d) are obtained using the control algorithms (13) and (14), respectively. Reference phase δ_1 is shown by the horizontal lines in (a), (b).

where I_l, I_k, and I_m are intensities of the corresponding optical fields at the photodetector location. Considering an optical field of the lth fiber collimator as a reference, represent Eq. (15) in the following equivalent form:

$$\begin{aligned} J_{l,k,m}[\delta_l(t),\delta_k(t),\delta_m(t)] &= I_l|1+\mu_k \exp[i\delta_k(t)-i\delta_l(t)]+\mu_m \exp[i\delta_m(t)-i\delta_l(t)]|^2 \\ &= 2I_l\{\mu_0^2+\mu_k \cos[\delta_k(t)-\delta_l(t)]+\mu_m \cos[\delta_m(t)-\delta_l(t)] \\ &\quad +\mu_k\mu_m \cos[\delta_k(t)-\delta_m(t)]\}, \end{aligned} \tag{16}$$

where $\mu_k^2=I_k/I_l$, $\mu_m^2=I_m/I_l$, and $\mu_0^2=(1+\mu_k^2+\mu_m^2)/2$ are the coefficients dependent on the intensities I_l, I_k, and I_m, and $\delta_k(t)-\delta_l(t)$ and $\delta_m(t)-\delta_l(t)$ are the differences between the phase errors of the reference, the lth, and the neighboring, kth and mth, subapertures. For simplicity we assumed that during the phase-locking process the piston phases Δ_j can be considered as stationary, so that $\delta_j(t)=u_j(t)+\Delta_j$, where $j=1,\ldots,N_{sub}$.

B. Phase Locking via Combined Metric Optimization

The most straightforward approach for the fiber-array phase locking using three-tail interference sensors is optimization of a combined metric $J_\Sigma(t)$ composed of electronically summarized signals (metric components) $J_{l,k,m}(\delta_l,\delta_k,\delta_m)$. Note that the combined metric $J_\Sigma(t)$ may also include additional metric components $J_{q,p}(\delta_q,\delta_p)$ obtained with two-tail interference sensors. Along with the three-tail sensors, these extra sensors can be used, for example, to interconnect fiber-array clusters, analogous to those in Fig. 4(d).

Consider a combined metric composed of K signals obtained using three-tail and M signals obtained with two-tail interference sensors:

$$J_\Sigma(t)=\sum_{m>k>l}^{K} J_{l,k,m}[\delta_l(t),\delta_k(t),\delta_m(t)]+\sum_{p>q}^{M} J_{q,p}[\delta_q(t),\delta_p(t)]. \tag{17}$$

From Eqs. (11) and (16) it is easy to see that the maximum values of terms $J_{l,k,m}(\delta_l,\delta_k,\delta_m)$ and $J_{q,p}(\delta_q,\delta_p)$ in Eq. (17) are achieved when the differences between the phase errors δ_k, δ_m, and δ_l for three-tail and between δ_q and δ_p for all two-tail sensors are equal or differ by an integer multiple of 2π. This means that in the case when all subapertures are interconnected, the global maximum of the combined metric (17) corresponds to the phase-locked state. Full interconnection means that differences $\delta_{k'}-\delta_{m'}$ between the phase errors for arbitrarily chosen subapertures k' and m' can be represented as a sum of the phase differences that are present in expression (17).

To illustrate the combined metric-optimization-based control, consider the fiber arrays with three-tail interference sensors, as shown in Fig. 7(a).

In the numerical simulations the following composed metric corresponding to three sensors is considered:

$$J_\Sigma=J_{1,2,3}(\delta_1,\delta_2,\delta_3)+J_{1,4,5}(\delta_1,\delta_4,\delta_5)+J_{1,6,7}(\delta_1,\delta_6,\delta_7). \tag{18}$$

The metric J_Σ is optimized using the SPGD control algorithm (13). The phase-locking performance is estimated

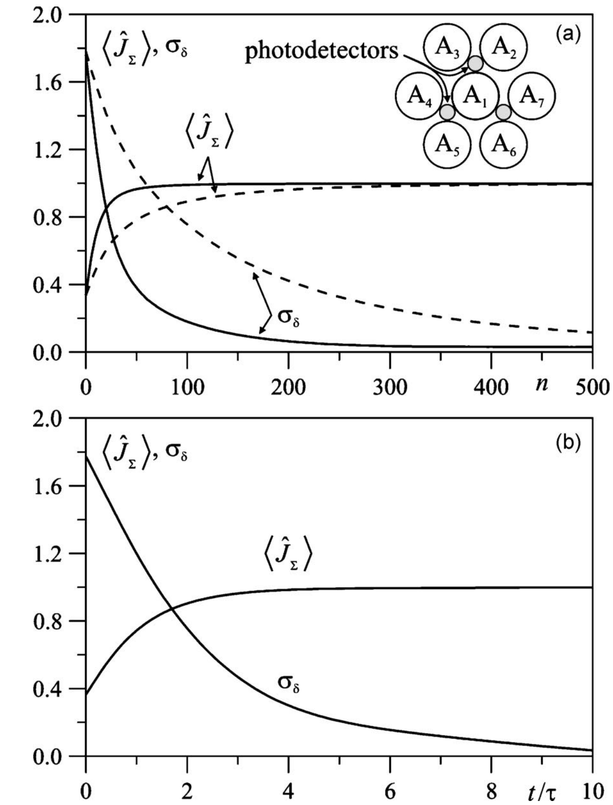

Fig. 7. Phase locking of a fiber array [shown in the insert in (a)] using local metrics obtained with three-tail sensors. Time dependences of the ensemble-averaged phase-locking performance measures $\langle \hat{J}_\Sigma(t) \rangle$ and $\sigma_\delta(t)$ using (a) optimization of the combined metric with SPGD (dashed lines) and local metrics with D-SPGD (solid lines) control algorithms and (b) the gradient-flow optimization algorithm (19).

using the normalized ensemble-averaged values $\langle \hat{J}_\Sigma \rangle \equiv \langle J_\Sigma \rangle / J_\Sigma^0$ and the phase-locking error standard deviation $\sigma_\delta(t)$ [see Eq. (6)]. The results are presented in Fig. 7(a) by the dashed lines.

Note that in most cases of the fiber-array systems examined, the control approach based on optimization of combined metrics [metrics (12), (17), and (18)] provided transitioning to the true phase-locked state. At the same time the numerical simulations demonstrated certain disadvantages of this control algorithm. In comparison with the parallel optimization of an array of local metrics discussed in Subsections 3.C–3.F for two-tail sensor networks, the use of combined metric optimization results in significantly slower convergence speed and on average lower accuracy in locking of piston phases.

This behavior can be explained by the potential existence of a number of local maxima of the combined metric, which is rather common for optimization of functions that are dependent on a large number of control variables.

C. Optimization of Three-Tail Local Metrics with D-SPGD Controller

Consider a phase-locking control algorithm that utilizes measurements obtained with three-tail sensors but provides better phase-locking accuracy and faster transitioning process convergence.

By way of example, assume that a fiber-array system is composed of seven fiber collimators and three sensors, as in the insert in Fig. 7(a). The local metrics $J_{1,2,3}(\delta_1,\delta_2,\delta_3)$, $J_{1,4,5}(\delta_1,\delta_4,\delta_5)$, and $J_{1,6,7}(\delta_1,\delta_6,\delta_7)$, measured by these sensors, depend on all seven phase errors $\delta_j, j=1,\ldots,7$. At the same time, for a fixed value of the reference phase δ_1, each local metric depends on only two independent phase errors. Since each of the metrics depends on the reference phase, independent maximization of the local metrics $J_{1,2,3}$, $J_{1,4,5}$, and $J_{1,6,7}$ results in locking of piston phases of all seven subapertures.

Maximization of the local metric can be performed either sequentially or in parallel using, for example, D-SPGD, multidithering, or heterodyne techniques.

The D-SPGD phase-locking control system for the fiber-array system with three-tail sensors as in Fig. 7(a) is composed of three identical subsystems that are described by the iterative equations similar to Eqs. (14) obtained for the two-tail sensors. The difference from the control rule (14) is that the identical metric perturbation value ($\Delta J_{1,2,3}^{(n)}$, $\Delta J_{1,4,5}^{(n)}$, or $\Delta J_{1,6,7}^{(n)}$) is used to update controls in two neighboring subapertures coupled by the corresponding three-tail sensor.

Dynamics of the phase-locking system based on D-SPGD optimization of local metrics obtained with three-tail sensors is illustrated in Fig. 7(a) by solid lines. In comparison with optimization of the combined metric (dashed lines), the phase-locking control based on local metric optimization provides significantly faster convergence speed.

D. Gradient-Flow Control with Three-Tail Sensing

Consider now phase locking based on the gradient-flow optimization of the local metrics measured with the three-tail sensors. The gradient components of the local metrics that are required for the gradient-flow optimization can be obtained using the multidithering technique. To illustrate, consider as an example three neighboring subapertures A_1, A_2, and A_3, corresponding to a single three-tail sensor in the fiber-array cluster with seven subapertures as in Fig. 7(a). The sensor output signal—the local metric $J_{1,2,3}(\delta_1,\delta_2,\delta_3)$—depends on the phase errors δ_1, δ_2, and δ_3 corresponding to these subapertures. Assume that single-frequency dither signals $a\sin(\omega t)$ and $a\cos(\omega t)$ are applied to the phase shifters corresponding to the second and third subapertures, thus resulting in modulation of the errors δ_2 and δ_3 and perturbations of the local metric $J_{1,2,3}(\delta_1,\delta_2,\delta_3)$. We assume that dithering amplitude a is small ($a \ll 1$) and that frequency ω exceeds the characteristic frequency bandwidth of piston phase variation in the fiber-array system.

It can be easily shown that using the heterodyne detection technique discussed in Section 2, one can electronically obtain the gradient components $\partial J_{1,2,3}(\delta_1,\delta_2,\delta_3)/\partial\delta_2$ and $\partial J_{1,2,3}(\delta_1,\delta_2,\delta_3)/\partial\delta_3$ of the metric $J_{1,2,3}(\delta_1,\delta_2,\delta_3)$. Note that the identical dithering signals can be used for measurements of the gradient components for the local metrics $J_{1,4,5}(\delta_1,\delta_4,\delta_5)$ and $J_{1,6,7}(\delta_1,\delta_6,\delta_7)$.

Similarly to Eqs. (5) for the fiber-array cluster with two-tail sensors, phase-locking control can be implemented using the gradient-flow optimization algorithm. For the fiber-array system with three sensors as in Fig.

7(a), the corresponding gradient-flow control is described by a set of the following equations:

$$\tau\frac{\mathrm{d}\delta_j(t)}{\mathrm{d}t}=\gamma_j\frac{\partial J_{1,j,j+1}}{\partial\delta_j}$$
$$=\gamma_j\{\sin[\delta_1(t)-\delta_j(t)]+\sin[\delta_{j+1}(t)-\delta_j(t)]\},\tag{19a}$$

$$\tau\frac{\mathrm{d}\delta_{j+1}(t)}{\mathrm{d}t}=\gamma_{j+1}\frac{\partial J_{1,j,j+1}}{\partial\delta_{j+1}}$$
$$=\gamma_{j+1}\{\sin[\delta_1(t)-\delta_{j+1}(t)]+\sin[\delta_j(t)-\delta_{j+1}(t)]\},\tag{19b}$$

where $j=2,4,6$ and $\{\gamma_j\}$ are the feedback gain coefficients. In derivation of the gradient components in Eqs. (19) we used the three-tail signal representation in the form of expression (16).

It is easy to show that equations (19) have a stable steady-state solution corresponding to the phase-locked state. The phase-locking dynamics in this system are illustrated in Fig. 7(b). The drawback of phase-locking control based on the gradient-flow optimization is related to an additional complexity of the control electronics that requires dithering and heterodyne filtering of the local metric gradients in comparison with the SPGD control.

5. PHASE LOCKING BASED ON FOCAL-PLANE BEAM-TAIL SENSORS

A. Focal-Plane Beam-Tail Interference

In our analysis we assumed that the size of photodetectors in the beam-tail interference sensors does not exceed the characteristic width w of either interference fringes for the two-tail or bright and dark spots for the three-tail sensor. In both cases value w can be estimated from the well-known expression $w=\lambda(f_0/l)$ describing the width of the interference fringes formed at a distance $f_0\sim f$ in Young's experiment with two point light sources that are separated by a distance l [38]. In our case l is the distance between two neighboring fiber tips, and f_0 is the distance between the fiber tips and the plane of the photodetectors, as in Fig. 4(a).

Note that in practical fiber-array systems the collimating lens focal distance f may exceed the separation distance l by only a few times (e.g., $f/l\sim 5$ in [3]). Correspondingly, the characteristic spatial scale w in these systems can be as small as a few micrometers. Since the size of photodetectors and the accuracy in their positioning should be smaller than w, practical implementation of the two- and three-tail interference sensors may present a challenging problem.

This technical problem can be overcome relatively easily by focusing beam-tail sections associated with the same sensor onto a common focal region (focal spot) using a specially designed combined focusing element (CFE) composed of an array of off-axis focusing elements (mirrors), as shown in Fig. 8(a) [39]. The focal spots are located a distance f_{CFE} from the CFE.

The off-axis focusing mirrors of the CFE can be made on (or integrated into) a common substrate with a set of

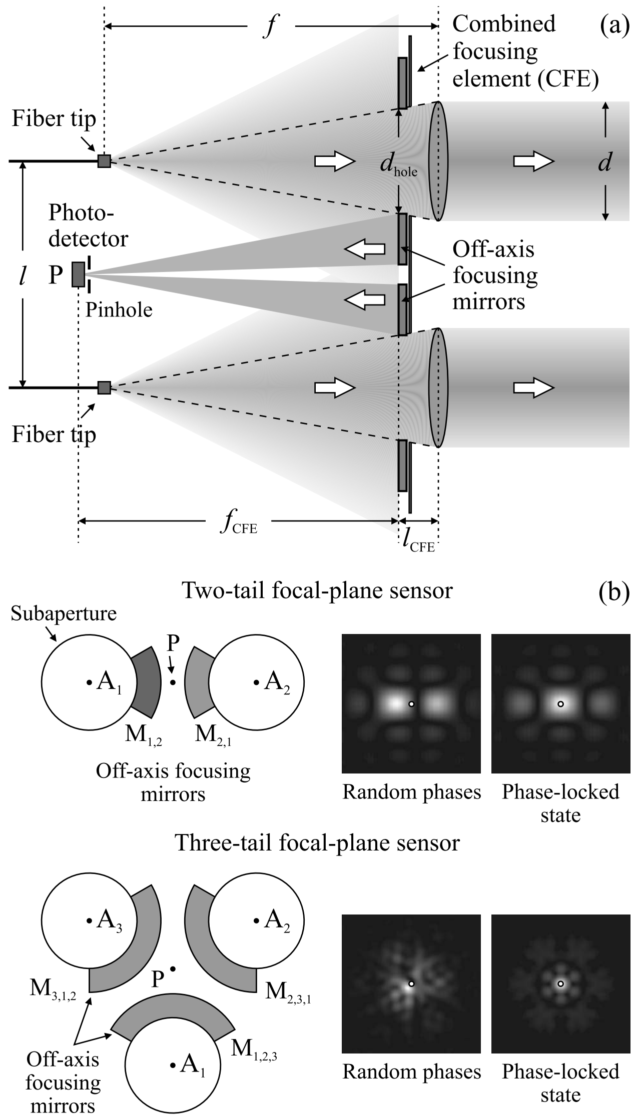

Fig. 8. Phase locking based on focal-plane beam-tail interference sensors: (a) notional schematic of the focal-plane beam-tail sensor and (b) geometries of off-axis focusing mirrors (M) corresponding to two- and three-tail focal-plane sensors. Grayscale images are examples of focal-plane intensity distributions obtained using the parameters of the experimental fiber array reported in [3]. Small circles at their centers show photodetector apertures.

holes that are large enough to prevent obscuration of the corresponding collimating lens aperture. This combined focusing element can be manufactured using, for example, the diffractive optics technique [39]. The CFE can be shifted back from the fiber-array pupil plane, thus creating additional space for the off-axis focusing mirror segments that can be required for fiber-array systems with high fill factor.

An example of the off-axis mirror geometry for two- and three-tail sensors is shown in Fig. 8(b). In this picture the off-axis focusing mirrors $M_{2,1}$ and $M_{1,2}$ of the neighboring subapertures A_1 and A_2 have a common focus at the point P a distance f_{CFE} from the CFE. Similarly, the mirrors $M_{1,2,3}$, $M_{2,3,1}$, and $M_{3,1,2}$ of the three-tail focal-plane sensor focus beam-tail sections of the corresponding subapertures A_1, A_2, and A_3 onto a common focal spot.

The characteristic size of the focal spot central lobe b_F is proportional to the distance f_{CFE} between the CFE and the plane of photodetectors and hence can be increased by arranging photodetectors at the rear plane of the fiber array. Examples of the intensity patterns formed at the focal plane of the two- and three-tail sensors are shown in Fig. 8(b) for both random and phase-locked states.

In the numerical simulations the CFE consists of an array of off-axis parabolic mirrors in the form of 60-deg annular segments for two-tail and 120-deg annular segments for three-tail focal-plane sensors. Note that other types of aspheric mirror surfaces, e.g., elliptical, can in principle be utilized as well. As seen from the focal-plane intensity patterns in Fig. 8(b), phase locking results in maximization of the peak intensity value at the photodetector location (white circles at the centers of grayscale images).

B. Phased Array with Focal-Plane Beam-Tail Sensors: Wave-Optics Model

In our previous analysis we assumed for simplicity that sensing of phase errors is performed using two- or three-tail sensors with infinitesimally small-size photodetectors (point-size detectors). This assumption allowed us to obtain simple analytical expressions describing the dependence of measured signals (metrics) on phase errors [see Eqs. (11) and (16)]. At the same time the actual size (aperture) of the photodetector or a pinhole located in front of it as in Fig. 8(a) can significantly affect phase-locking system performance, including control process stability, phase-locking bandwidth, and accuracy.

In this and the following subsection we consider a more realistic case of obscuration-free pupil-plane phase locking using focal-plane beam-tail sensors with finite-size photodetectors. In this case the dependence of the measured signals (metrics) on phase errors cannot be obtained analytically, and therefore performance analysis of phase-locking systems requires wave-optics simulations of the entire optical train from the fiber tips to the off-axis focusing element and further to the plane of the photodetectors.

As an example of such analysis, consider the coherent array of $N_{sub}=7$ fiber collimators as in Fig. 1(a). Assume that the complex amplitudes of the outgoing beamlets' optical fields right before the collimating lenses can be represented in the form of diverging Gaussian beams propagating along the optical axis (oz direction) centered at the coordinates $\mathbf{r}_j$, that is,

$$A_j(\mathbf{r}-\mathbf{r}_j,t)=A_0(\mathbf{r}-\mathbf{r}_j)\exp[-ik|\mathbf{r}-\mathbf{r}_j|^2/2f+i\delta_j(t)] \quad (j=1,\ldots,N_{sub}), \tag{20}$$

where $A_0(\mathbf{r}-\mathbf{r}_j)=A_0\exp(-|\mathbf{r}-\mathbf{r}_j|^2/a_0^2)$, a_0 is the Gaussian beam characteristic width parameter, $A_0>0$ is a constant, f is the collimating lens focal distance, $k=2\pi/\lambda$, and λ is the wavelength.

To simplify the analysis, assume that the combined focusing element is located directly behind the fiber-array collimating lenses at the plane $z=0$ and focuses the tail sections of the divergent Gaussian beam to the distance f_{CFE}.

Consider a single off-axis mirror segment that focuses the lth region of the jth beam tail to the kth photodetector located at the plane $z=-f_{\mathrm{CFE}}$ with the center at the coordinate vector $\mathbf{r}_k$. The reflection coefficient of this off-axis mirror segment can be described by a stepwise function $V_l(\mathbf{r}-\mathbf{r}_k)$ that equals unity inside the mirror segment region Ω_l and zero otherwise. In the numerical simulations this region is defined by an annular segment adjacent to the jth subaperture with the outer diameter l and the inner diameter d.

With the introduced notation, the complex transfer function of the off-axis mirror element can be represented in the form

$$T_l^{\mathrm{CFE}}(\mathbf{r},\mathbf{r}_j,\mathbf{r}_k,t)=V_l(\mathbf{r}-\mathbf{r}_k)\exp[-i\varphi(\mathbf{r}-\mathbf{r}_j,f)+i\varphi(\mathbf{r}-\mathbf{r}_k,f_{\mathrm{CFE}})], \tag{21}$$

where $\varphi(\mathbf{r},f)=-k|\mathbf{r}|^2/(2f)$ is the parabolic phase of the Gaussian beam (beamlet) at distance f from the fiber tip. In this expression, the presence of the phase term $-\varphi(\mathbf{r}-\mathbf{r}_j,f)$ in the transfer function (21) leads to cancellation of the parabolic phase of the divergent Gaussian beamlet at the CFE plane, while the second phase term $\varphi(\mathbf{r}-\mathbf{r}_k,f_{\mathrm{CFE}})$ in Eq. (21) results in formation of an optical wave reflected from the mirror segment with convergent parabolic phase with focus at the point $(\mathbf{r}_k,z=-f_{\mathrm{CFE}})$, the point of the photodetector location.

The complex amplitude $A_l^{\mathrm{CFE}}(\mathbf{r},\mathbf{r}_j,\mathbf{r}_k,t)$ of the jth beam tail reflected off the lth mirror at the plane $z=0$ toward the kth photodetector is therefore given by the following expression:

$$\begin{aligned} A_l^{\mathrm{CFE}}(\mathbf{r},\mathbf{r}_j,\mathbf{r}_k,t) &= A_0(\mathbf{r}-\mathbf{r}_j)V_l(\mathbf{r}-\mathbf{r}_k) \times \exp[i\varphi(\mathbf{r}-\mathbf{r}_k,f_{\mathrm{CFE}})+i\delta_j(t)] \\ &\equiv \tilde{A}_l^{\mathrm{CFE}}(\mathbf{r},\mathbf{r}_j,\mathbf{r}_k)\exp[i\delta_j(t)], \end{aligned} \tag{22}$$

where $\tilde{A}_l^{\mathrm{CFE}}(\mathbf{r},\mathbf{r}_j,\mathbf{r}_k)$ is the time-independent component of the beam-tail complex amplitude. At the photodetector plane $z=-f_{\mathrm{CFE}}$, the corresponding complex amplitude can be expressed through the Fresnel diffraction integral [38] as

$$\begin{aligned} A_l^{\mathrm{PD}}(\mathbf{r},\mathbf{r}_j,\mathbf{r}_k,t) &= -\frac{ik}{2\pi f_{\mathrm{CFE}}}\exp(ikf_{\mathrm{CFE}})\int A_l^{\mathrm{CFE}}(\mathbf{r}',\mathbf{r}_j,\mathbf{r}_k,t) \times\exp[-i\varphi(\mathbf{r}'-\mathbf{r},f_{\mathrm{CFE}})]\mathrm{d}\mathbf{r}' \\ &\equiv \tilde{A}_l^{\mathrm{PD}}(\mathbf{r},\mathbf{r}_j,\mathbf{r}_k)\exp[i\delta_j(t)], \end{aligned} \tag{23}$$

where $\tilde{A}_l^{\mathrm{PD}}(\mathbf{r},\mathbf{r}_j,\mathbf{r}_k)$ is the time-independent optical field component.

The optical field at the kth photodetector represents the sum of all the contributing beam tails. For both the two- and the three-tail interference sensors considered, each beamlet contributes only one tail section to this field. Correspondingly, in Eq. (23) index l can be associated with one of the beamlet indices j and hence can be omitted. The intensity distribution at the plane of the kth photodetector is then given by

$$I_k^{\mathrm{PD}}(\mathbf{r},t) = \left| \sum_{l_k=1}^{N_{ng}} \tilde{A}_{l_k}^{\mathrm{PD}}(\mathbf{r},\mathbf{r}_k)\exp[i\delta_{l_k}(t)] \right|^2, \tag{24}$$

where $N_{ng}=2$ for the two-tail and $N_{ng}=3$ for the three-tail focal-plane sensors. The indices l_k in Eq. (24) identify the neighboring subapertures that contribute their beam-tail sections to the optical field at the plane of kth photodetector. The signal (local metric) $J_k(t)$ measured by the kth photodetector can be obtained by integrating Eq. (24) over the finite aperture of radius b_{PD} centered at $\mathbf{r}_k$:

$$J_k(t) = \int_{S_{\mathrm{PD}}} I_k^{\mathrm{PD}}(\mathbf{r},t)\mathrm{d}^2(\mathbf{r}-\mathbf{r}_k), \tag{25}$$

where $S_{\mathrm{PD}}=\pi b_{\mathrm{PD}}^2$. It is easy to show that for the point-size photodetector the local metric value obtained from Eq. (25) is equivalent to Eq. (16) used in the analysis in Section 4.

C. Wave-Optics Simulations of Phase-Locking Process Performance

Consider the results of wave-optics numerical simulations of the phase-locking system based on local metrics optimization (D-SPGD controller) for the fiber-array system composed of seven fiber collimators as in Fig. 4(b) with three-tail focal-plane sensors. The parameters of the system correspond to the fiber-array system described in [3]: $d=27$ mm, $a_0=0.45d$, $l=1.37d$, $f=5.5d$, $\lambda=1.06$ μm. The CFE consists of $N_{sub}=7$ subapertures (circular holes of diameter d) and nine off-axis parabolic mirror segments in the form of 120-deg annular zones, as shown in Fig. 9(a). Each three adjacent mirrors, denoted in the figure by the areas with identical fills, have a common focus at $f_{\mathrm{CFE}}=8.9d$. The CFE is located at the fiber-array system pupil plane ($l_{\mathrm{CFE}}=0$).

In the numerical simulations, the metrics (25) are optimized using the D-SPGD control algorithm described in Subsection 4.C. Similarly to the analysis for the point-size photodetectors, the phase-locking performance is estimated using both the normalized ensemble-averaged parameter $\langle\hat{J}_\Sigma\rangle=\langle J_\Sigma\rangle/J_\Sigma^0$ and the phase-locking error standard deviation σ_δ [see Eq. (6)], where $J_\Sigma=J_1+J_2+J_3$ and J_Σ^0 is the metric value corresponding to zero phase errors. Averaging is performed over 100 random realizations of initial piston phases.

The numerical simulation results are shown in Fig. 9(b) for the point-size photodetector ($b_{\mathrm{PD}}=0$, solid lines) and for the photodetectors of two different sizes: $b_{\mathrm{PD}}=b_{\mathrm{Airy}}/2$ (dashed lines), and $b_{\mathrm{PD}}=b_{\mathrm{Airy}}$ (dot-dashed lines), where $b_{\mathrm{Airy}}=1.22\lambda(f_{\mathrm{CFE}}/l)$ is the Airy disk radius for the focusing element with aperture of diameter l (the outer diameter of the mirror segment) and focal distance f_{CFE}. As can be seen, the normalized metrics $\langle\hat{J}_\Sigma\rangle$ converge to their optimal value independently of the size of the photodetector. Nevertheless, the phase-locking error σ_δ—the true characteristic of phase-locking performance—is quite sensitive to the photodetector size. The achieved value of σ_δ increases with the increase of the photodetector aperture size.

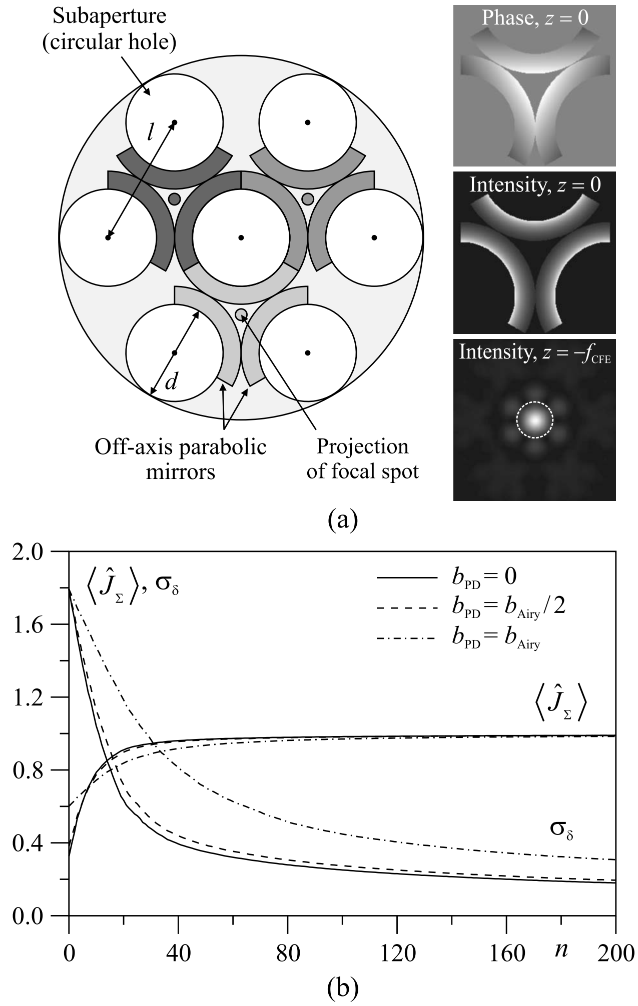

Fig. 9. Phase locking with focal-plane beam-tail sensors: (a) schematic of the combined focusing element for three-tail focal-plane sensing used in numerical simulations (left), phase pattern of the complex transfer function argument in Eq. (21) corresponding to three off-axis parabolic mirrors with a common focal spot (top-right), intensity distribution of the beam tails at the CFE plane (middle-right), and intensity distribution at the focal plane (bottom-right); (b) metrics $\langle\hat{J}_\Sigma\rangle$ and σ_δ versus the iteration number n for three different photodetector aperture radii: $b_{\mathrm{PD}}=0$ (solid lines), $b_{\mathrm{PD}}=b_{\mathrm{Airy}}/2$ (dashed lines), and $b_{\mathrm{PD}}=b_{\mathrm{Airy}}$ (dot-dashed lines). The dashed circle in (a) indicates the Airy disk of diameter $2b_{\mathrm{Airy}}$.

6. CONCLUSION

In this paper we introduced and analyzed several control techniques and system architectures that can be used for phase locking of the outgoing laser beams (beamlets) that are generated at the pupil plane of a coherent fiber-collimator array (pupil-plane phase locking). The techniques considered are based on sensing of piston phases of the outgoing beamlets using an interference of periphery (tail) sections of these beams prior to these tail sections being clipped by the fiber-collimator lens apertures. Since these beam-tail interference sensors are located outside the fiber-collimator optical train, the phase-locking methods do not require installation of any external optical elements at the optical train of the operating fiber-array system. From this viewpoint the fiber-collimator array with the obscuration-free phase-locking system described can be considered as a new type of a coherent laser beam director system that does not require a bulky optical beam expander (telescope) in order to increase the outgoing laser beam aperture. This conformal beam director can also include additional capabilities for adaptive optics compensation of phase aberrations caused by the outgoing conformal beam that are directly integrated into each fiber collimator of the fiber array.

Among potential challenges for practical implementation of the obscuration-free pupil-plane phase-locking techniques described, we can mention strict requirements on positioning and alignment of photodetectors in the two- and three-tail interference sensors as well as the potential presence of additional static piston phase aberrations related, for example, to non-common path errors caused by the variations in the optical thickness of the collimating lenses and/or non-optimal positioning of the beam-tail focusing mirror elements. These unsensed static phase shifts cannot be detected by the beam-tail interference sensors. Nevertheless, they can be evaluated by measuring piston phases of the outgoing beamlets during the closed-loop operation of the phase-locking system described. These measurements require an external wavefront sensor placed in front of the fiber array, such as for example in Fig. 2. However, after these measurements are completed, this external wavefront sensor can be removed. The measured static phase errors can be precompensated, e.g., by using glass plates with calibrated thickness or liquid crystal (LC) phase-shifting elements (LC cells) that are positioned in the optical train of the outgoing beamlets right after they exit the collimating lenses [see Fig. 1(a)]. Another option that does not require an external compensating element is related to calibrated, intentional displacements of the beam-tail-sensor photodetectors. In the operating phase-locking system, these displacements result in the appearance of additional phase shifts of the outgoing beamlets, as discussed in Subsection 3.A [phase shifts ζ in Eq. (3)]. Optimal positioning of the photodetectors aiming at the precompensation of these phase shifts can be performed once, using an external wavefront sensor that is no longer required during the fiber-array system operation.

ACKNOWLEDGMENTS

This work was supported in part by Cooperative Agreement (CA) W911NF-06-2-0009 between the U.S. Army Research Laboratory (ARL) and the University of Maryland, College Park, and by CA W911NF-09-2-0040 between ARL and the University of Dayton.

REFERENCES

1. J. R. Leger, J. Nilsson, J. P. Huignard, A. P. Napartovich, T. M. Shay, and A. Shirakawa, eds., Special issue, "Laser beam combining and fiber laser systems," IEEE J. Sel. Top. Quantum Electron. **15**, 237–470 (2009).
2. K. H. Kudielka, A. Kalmar, and W. R. Leeb, "Design and breadboarding of a phased telescope array for free-space laser communications," in *Proceedings of IEEE International Symposium on Phased Array Systems and Technology* (IEEE, 1996), pp. 419–424.
3. M. A. Vorontsov, T. Weyrauch, L. A. Beresnev, G. W. Carhart, L. Liu, and K. Aschenbach, "Adaptive array of phase-locked fiber collimators: Analysis and experimental demonstration," IEEE J. Sel. Top. Quantum Electron. **15**, 269–280 (2009).
4. T. Y. Fan, "Laser beam combining for high-power, high-radiance sources," IEEE J. Sel. Top. Quantum Electron. **11**, 567–577 (2005).
5. S. J. Augst, J. K. Ranka, T. Y. Fan, and A. Sanchez, "Beam combining of ytterbium fiber amplifiers (Invited)," J. Opt. Soc. Am. B **24**, 1707–1715 (2007).
6. C. D. Nabors, "Effects of phase errors on coherent emitter arrays," Appl. Opt. **33**, 2284–2289 (1994).
7. P. Sprangle, A. Ting, J. Penano, R. Fischer, and B. Hafizi, "Incoherent combining and atmospheric propagation of high-power fiber lasers for directed-energy applications," IEEE J. Quantum Electron. **45**, 138–148 (2009).
8. A. Kobyakov, M. Sauer, and D. Chowdhury, "Stimulated Brillouin scattering in optical fibers," Adv. Opt. Photon. **2**, 1–59 (2010).
9. V. I. Kovalev, Department of Physics, Heriot-Watt University, Edinburgh EH14 4AS, UK (personal communication, 2010).
10. P. F. McManamon, P. J. Bos, M. J. Escuti, J. Heikenfeld, S. Serati, H. Xie, and E. A. Watson, "A review of phased array steering for narrow-band electrooptical systems," Proc. IEEE **97**, 1078–1096 (2009).
11. T. H. Loftus, A. M. Thomas, P. R. Hoffman, M. Norsen, R. Royse, A. Liu, and E. C. Honea, "Spectrally beam-combined fiber lasers for high-average-power applications," IEEE J. Sel. Top. Quantum Electron. **13**, 487–497 (2007).
12. A. Sevian, O. Andrusyak, I. Ciapurin, V. Smirnov, G. Venus, and L. Glebov, "Efficient power scaling of laser radiation by spectral beam combining," Opt. Lett. **33**, 384–386 (2008).
13. J. R. Leger, "External methods of phase locking and coherent beam addition of diode lasers," in *Surface Emitting Semiconductor Lasers and Arrays*, G. A. Evans and J. M. Hammer, eds. (Academic, 1993), pp. 379–433.
14. M. Minden, "Coherent coupling of a fiber amplifier array," in *Thirteenth Annual Solid State and Diode Laser Technology Review*, SSDLTR 2000 Tech. Digest (U. S. Air Force Research Laboratory, 2000).
15. A. F. Glova, "Phase locking of optically coupled lasers," Quantum Electron. **33**, 283–306 (2003).
16. J. Anderegg, S. J. Brosnan, M. E. Weber, H. Komine, and M. G. Wickham, "8-W coherently phased 4-element fiber array," Proc. SPIE **4974**, 1–6 (2003).
17. J. Anderegg, S. Brosnan, E. Cheung, P. Epp, D. Hammons, H. Komine, M. Weber, and M. Wickham, "Coherently coupled high-power fiber arrays," Proc. SPIE **6102**, 61020U (2006).
18. J. E. Kansky, C. X. Yu, D. V. Murphy, S. E. J. Shaw, R. C. Lawrence, and C. Higgs, "Beam control of a 2D polarization maintaining fiber optic phased array with high-fiber count," Proc. SPIE **6306**, 63060G (2006).
19. M. A. Vorontsov and S. L. Lachinova, "Laser beam projection with adaptive array of fiber collimators. I. Basic considerations for analysis," J. Opt. Soc. Am. A **25**, 1949–1959 (2008).
20. S. L. Lachinova and M. A. Vorontsov, "Laser beam projection with adaptive array of fiber collimators. II. Analysis of atmospheric compensation efficiency," J. Opt. Soc. Am. A **25**, 1960–1973 (2008).
21. R. A. Motes and R. W. Berdine, *Introduction to High Power Fiber Lasers* (Directed Energy Professional Society, 2009).
22. B. Lei and Y. Feng, "Phase locking of an array of three fiber lasers by an all-fiber coupling loop," Opt. Express **15**, 17114–17119 (2007).
23. Z. Chen, J. Hou, P. Zhou, X. Wang, X. Xu, Z. Jiang, and Z. Liu, "Mutual injection locking and coherent combining of three individual fiber lasers," Opt. Commun. **282**, 60–63 (2009).
24. EOSPACE, http://www.eospace.com/.
25. H. Bruesselbach, D. C. Jones, M. S. Mangir, M. Minden, and J. L. Rogers, "Self-organized coherence in fiber laser arrays," Opt. Lett. **30**, 1339–1341 (2005).
26. E. L. Wooten, K. M. Kissa, A. Yi-Yan, E. J. Murphy, D. A. Lafaw, P. F. Hallemeier, D. Maack, D. V. Attanasio, D. J.

Fritz, G. J. McBrien, and D. E. Bossi, “A review of lithium niobate modulators for fiber-optic communications systems,” IEEE J. Sel. Top. Quantum Electron. **6**, 69–82 (2000).

27. J. Ichikawa, “$LiNbO_3$ based optical devices for fiber communication,” J. China Univ. Posts Telecommun. **16**, 12–15 (2009).
28. T. R. O’Meara, “The multidither principle in adaptive optics,” J. Opt. Soc. Am. **67**, 306–315 (1977).
29. T. M. Shay, “Theory of electronically phased coherent beam combination without a reference beam,” Opt. Express **14**, 12188–12195 (2006).
30. M. A. Vorontsov, G. W. Carhart, and J. C. Ricklin, “Adaptive phase-distortion correction based on parallel gradient-descent optimization,” Opt. Lett. **22**, 907–909 (1997).
31. M. A. Vorontsov, G. W. Carhart, M. Cohen, and G. Cauwenberghs, “Adaptive optics based on analog parallel stochastic optimization: analysis and experimental demonstration,” J. Opt. Soc. Am. A **17**, 1440–1453 (2000).
32. W. S. Levine, ed., *The Control Handbook* (CRC Press, 1996).
33. M. A. Vorontsov and V. I. Shmal’hauzen, *Principles of Adaptive Optics* (Nauka, 1985).
34. B. M. ter Haar Romey, ed., *Geometry-Driven Diffusion in Computer Vision* (Kluwer Academic, 1994).
35. E. W. Justh, M. A. Vorontsov, G. W. Carhart, L. A. Beresnev, and P. S. Krishnaprasad, “Adaptive optics with advanced phase-contrast techniques. II. High-resolution wave-front control,” J. Opt. Soc. Am. A **18**, 1300–1311 (2001).
36. W. H. Press, S. A. Teukolsky, W. T. Vetterling, and B. P. Flannery, *Numerical Recipes: The Art of Scientific Computing*, 3rd ed. (Cambridge University Press, 2007).
37. M. A. Vorontsov, “Decoupled stochastic parallel gradient descent optimization for adaptive optics: Integrated approach for wave-front sensor information fusion,” J. Opt. Soc. Am. A **19**, 356–368 (2002).
38. M. Born and E. Wolf, *Principles of Optics*, 6th ed. (Pergamon, 1980).
39. M. A. Vorontsov, G. W. Carhart, L. A. Beresnev, T. Weyrauch, and S. L. Lachinova, “Phase-locking system for fiber collimator array,” Invention Disclosure, U.S. Army Research Laboratory, University of Maryland (June 2009).